Localised pattern formation in a model for dryland vegetation

J.H.P. Dawes and J.L.M. Williams

Department of Mathematical Sciences, University of Bath,
Claverton Down, Bath BA2 7AY, UK

October 5, 2015

Abstract

We analyse the model for vegetation growth in a semi-arid landscape proposed by von Hardenberg et al [*Phys. Rev. Lett.* 87:198101, 2001], which consists of two parabolic partial differential equations that describe the evolution in space and time of the water content of the soil and the level of vegetation. This model is a generalisation of one proposed by Klausmeier but it contains additional terms that capture additional physical effects. By considering the limit in which the diffusion of water in the soil is much faster than the spread of vegetation, we reduce the system to an asymptotically simpler parabolic-elliptic system of equations that describes small amplitude instabilities of the uniform vegetated state. We carry out a thorough weakly nonlinear analysis to investigate bifurcations and pattern formation in the reduced model. We find that the pattern forming instabilities are subcritical except in a small region of parameter space.

In the original model at large amplitude there are localised solutions, organised by homoclinic snaking curves. The resulting bifurcation structure is well known from other models for pattern forming systems. Taken together our results describe how the von Hardenberg model displays a sequence of (often hysteretic) transitions from a non-vegetated state, to localised patches of vegetation that exist with uniform low-level vegetation, to periodic patterns, to higher-level uniform vegetation as the precipitation parameter increases.

Keywords: semi-arid environment; bifurcation; localised state; homoclinic snaking;

1 Introduction

Desertification is a specific type of land degradation in which an already dry landscape become progressively more arid. It is characterised by a combined loss of water and plant biomass making the land barren and unable to support new plant life. It is an increasingly relevant issue in society since rapid population growth necessitates ever more effective use of land for agriculture. Desertification can be caused directly by human activities (e.g. overcultivation which serves to deplete the soil of nutrients and make it more difficult for new plants to grow) or indirectly, e.g. via overgrazing which actively removes plant biomass through herbivory. To a lesser extent, it may also result from climate change or geological factors.

The most successful method of combatting desertification is afforestation: the planting of trees and shrubs. This serves to prevent desertification in several ways. Studies (e.g. [17, 27]) have shown that an increase in vegetation cover will cause a significant decrease in soil erosion rates; the retention of the topsoil layer encourages plant growth. Another method used to avoid soil erosion is to fixate the soil by planting trees in lines in order to form windbreaks. Methods of combatting desertification are expensive and often need to be planned over long timescales. Governments of countries affected by this problem are keen to find ways of identifying areas at high risk so that plans can be more effectively targeted. Such methods are of particular interest to the Israeli government since 90% of Israel is classed as semi-arid or arid and 60% is already covered by the Negev Desert. The term semi-arid is applied to describe ecosystems with an annual rainfall of 250-500mm, these are estimated to cover 30% of the Earth's land surface [25].

The study of vegetation patches in semi-arid landscapes has long been of interest to theoretical biologists and land ecologists and, in more recent years, applied mathematicians. The reason for this is that a naturally occuring feature of such landscapes is the formation of vegetation patterns. These organic structures are often difficult to see from the ground and were first observed in 1950 in aerial photographs of sub-saharan Africa [15, 16]. Since then similar patterns have been observed in a variety of semi-arid regions including parts of Australia [14] and Mexico [19]. It is thought that these patterns hold the key to understanding the desertification process. If one were able to accurately model the development of the vegetation patterns in a certain region, one could use this to make predictions about the state of the land in the future. Different scenarios could be explored, for instance the effect of introducing different plans to combat desertification or alternatively the outcome if no intervention is planned.

This ability to predict and control desertification is therefore the motivation behind deriving mathematical models which encapsulate the behaviour of vegetation in semi-arid environments. A number of mathematical models have been put forward that describe the behaviour of vegetation in semi-arid environments and in particular attempt to capture the pattern formation in these ecosystems. These models are typically examples of reaction-diffusion equations involving two ore more physical variables. One of the first such systems that models pattern formation in semi-arid landscapes was introduced by Klausmeier [12], and is a pair of reaction-diffusion equations for soil water content and biomass. This model has been further developed in a number of publications. The model proposed by von Hardenberg et al. [9] will be used as the starting point for the mathematical analysis carried out in this paper.

More complicated models which include a third equation that describes the behaviour of surface water, were proposed by HilleRisLambers et al. [10] and Gilad et al. [7]. The rationale for treating surface water as a separate variable is that rainfall in semi-arid environments has a tendency to fall in short, sharp showers. This causes a layer of water to build up above ground level during a period of rainfall since infiltration rates are slower than precipitation rates. We will not consider these three-component models in any detail in the present paper, but it would be natural to include them in future work.

1.1 The Klausmeier model

We start by reviewing the original model put forward by Klausmeier [12]. The variables $N(\mathbf{X}, T)$ and $W(\mathbf{X}, T)$, represent local (non-negative) densities of plant biomass and soil water respectively; they depend on $\mathbf{X} = (X, Y)$, the surface coordinates, and time T. Klausmeier proposed a reaction-diffusion type model as follows:

$$
\begin{aligned}
N_T &= RJWN^2 - MN + D\nabla^2 N & (1) \\
W_T &= P - LW - RWN^2 + VW_X & (2)
\end{aligned}
$$

In (1) the term $RJWN^2$ (where R and J are positive constants) describes the uptake of water through the roots of the plants and its use to grow additional plant mass. In general Klausmeier proposes a plant growth / water uptake term proportional to $G(W)F(N)N$, where $G(W)$ is the functional response describing how biomass increases as a function of soil water level W and $F(N)$ is a function that describes how increasing biomass also increases water filtration through the soil. This latter effect is due to the roots of shrubs and grasses breaking down the top crust of the soil, allowing increased water filtration. It is therefore evident that $F(N)$ and $G(W)$ should be increasing functions. R is a constant of proportionality and J describes the yield of biomass per unit of soil water consumed. In the simplest case, the functions $G(W)$ and $F(N)$ can be taken to be linear; $G(W) = W$ and $F(N) = N$. Klausmeier asserts that the form of these functions makes little qualitative difference to the behaviour of the model. Loss of plant biomass occurs through mortality and herbivory at rate proportional to the local level of biomass N, with a constant M. Finally the diffusion term $D\nabla^2 N$ models the isotropic spatial spread of plants through seed dispersal or clonal reproduction.

Equation (2) describes the variation of the soil water content in time and space. The source term P represents water added to the system, assumed to be added uniformly in space via precipitation, and constant in time. Similarly, the term $-LW$ describes evaporation (L is another positive parameter). The final term VW_X in the soil water equation describes the effect of sloping ground: soil water is transported downhill.

A nondimensional form of equations (1) and (2) can be obtained by introducing the following scalings:

$$
\begin{aligned}
(W, N) &= R^{-1/2}L^{1/2}(J^{-1}w, n), & (X, Y) &= L^{-1/2}D^{1/2}(x, y), & T &= L^{-1}t, & (3) \\
P &= R^{-1/2}J^{-1}L^{3/2}p, & M &= Lm, & V &= L^{1/2}D^{1/2}v,
\end{aligned}
$$

where the rescaled variables $n(\mathbf{x}, t)$ and $w(\mathbf{x}, t)$ describe the (dimensionless) spatiotemporal variations of plant biomass and soil water, respectively. The nondimensionalisation procedure essentially scales out the parameters D, J, L and R. When nondimensionalised, the Klausmeier model becomes:

$$n_t = wn^2 - mn + \nabla^2 n, \tag{4}$$
$$w_t = p - w - wn^2 + vw_x, \tag{5}$$

with p, m, and v remaining as parameters. Several authors, for example Kealy & Wollkind [11], Zelnick et al [26], and Siteur et al [24], study a modified version of (4) - (5) in which the soil water equation (5) is augmented by a diffusion term in the form $D\nabla^2 w$ and the advection term vw_x is removed.

To give an idea of the possible further extensions of the Klausmeier model which have been studied, we mention very briefly the model proposed by HilleRisLambers et al [10], see also [20], which treats surface water, described by a third variable $H(\mathbf{X}, T)$, as an additional field, evolving separately from the ground water. HilleRisLambers et al [10] proposed the (dimensional) model:

$$N_T = \frac{W}{W+1} N - bN + D_N \nabla^2 N,$$
$$W_T = \frac{N + W_H}{N+1} H - \frac{W}{W+1} kN - rW + D_W \nabla^2 W,$$
$$\frac{cg_{max}}{\alpha} H_T = P_S - \frac{N + W_H}{N+1} H + \nabla^2 H,$$

which contains a number of substantial modelling differences. The water uptake from the soil to the plant biomass is now modelled by a term whose dependence on W saturates at large W. Similarly, the flow of water from the surface into the soil is modelled by a term depending on N, but again with a rate that varies between the constant W_H for bare ground (i.e. when $N = 0$) and saturates to unity at large N. Diffusion of all three quantities is anticipated, although with different diffusion coefficients for each variable. Further discussion of a number of models in the literature is given by Zelnik et al [26].

The structure of the remainder of this paper is as follows. In section 2 we describe the structure of the von Hardenberg model which combines a number of effects discussed above. We summarise the uniform states supported by this model and we investigate their susceptability to pattern forming instabilities. We then present a rescaling that simplifies this model further. Section 3 derives the reduced model and sets out the weakly-nonlinear analytic progress that we are able to make. We present also numerical solutions obtained via continuation, using the well-known software package AUTO [6]. In section 4 we return to the full von Hardenberg model and present results showing the existence of localised states and homoclinic snaking. Section 5 concludes the paper.

2   The von Hardenberg model

In this section we consider in significant detail, the model introduced by von Hardenberg et al [9], see also recent work by Gowda et al [8] on two dimensional pattern selection in this model. The von Hardenberg model is fundamentally very similar to the Klausmeier model; we explore the consequences and significance of the modifications and additional parameters that the von Hardenberg model contains.

The von Hardenberg model takes the form

$$n_t = \frac{\gamma w}{1 + \sigma w} n - n^2 - \mu n + \nabla^2 n, \tag{6}$$
$$w_t = p - (1 - rn)w - w^2 n + \delta \nabla^2 (w - \beta n) - \nu(w - \alpha n)_x, \tag{7}$$

which is already in nondimensional form. Similar to the Klausmeier model, it is a pair of partial differential equations in the non-negative quantities $n(\mathbf{x}, t)$ and $w(\mathbf{x}, t)$, biomass and water respectively, which are functions of space $\mathbf{x}$ and time t.

In the biomass equation (6) the terms are a mixture of familiar and new ones. As before, we have a negative term $-\mu n$ corresponding to loss of plant matter and a diffusion term $\nabla^2 n$ accounting for the spread of plants. However this time the growth of biomass is given by $\gamma wn/(1+\sigma w)$. This form is chosen so that growth occurs at a rate that grows linearly with w for dry soil. We also notice the presence of a negative quadratic term $-n^2$ which allows for saturation of the soil due to limited nutrients.

In the equation for groundwater density (7), the first term p stands for precipitation and is equivalent to the variable p in Klausmeier's equation (5). The second term $-(1 - rn)w$ represents a loss of water

due to evaporation and is the analogue of $-w$ in (5). Unlike the Klausmeier model, it includes the effect of shading by plant matter with the $-rn$ expression, which acts to decrease the amount of water lost where there is biomass protecting the soil. Clearly this term becomes unphysical when $n > 1/r$ since it then would turn from a sink into a source term.

The $-w^2 n$ term accounts for local uptake of water through the roots and is in effect similar to the $-wn^2$ term in (5). The surface runoff term $\nu(w - \alpha n)_x$ models the effect of preferential advection of soil water down a slope, where ν is the downhill runoff velocity. The difference between this term and the vw_x term in (5) is that the quantity being differentiated is now $w - \alpha n$ as opposed to just w. This takes into account the drop in runoff in areas of higher vegetation due to increased infiltration. In this paper we consider only the case of level ground and set $\nu = 0$ throughout the following analysis. This implies also that the parameter α does not appear in the remainder of the paper.

There is one additional term in (7) not present in (5), namely $\delta \nabla^2 (w - \beta n)$ which models diffusion of water through the soil. Comparing the two models, it is clear that the extensions by von Hardenberg et al. are intended to capture additional physical effects and feedbacks between the biomass and the soil water variables which have natural physical interpretations, but which are not present in the Klausmeier model. In particular, while keeping the level of precipitation p as our primary bifurcation parameter, we will focus on the behaviour of the von Hardenberg model as the parameters r and β are varied since these describe the new physical effects and feedbacks.

2.1 Uniform states

In this subsection we summarise the existence of uniform states for the von Hardenberg model (6) - (7) in one spatial dimension. There are two possible kinds of uniform state: either $n = 0$ and $w = p$ everywhere, corresponding to a vegetation-free equilibrium, or a state with $n = n_0 \neq 0$, $w = w_0$ constant. von Hardenberg et al refer to these as the 'bare state' $\mathcal{B}$ and a uniform vegetation state $\mathcal{V}$, respectively. Note that there is only one possible $\mathcal{B}$ state, but that more than one $\mathcal{V}$ state may exist for a particular set of parameter values.

To investigate the linear stability of the bare state $n = 0$; $w = p$ we write $n = n_1$, $w = p + w_1$, substitute into (6) - (7) and linearise in n_1, w_1 to obtain

$$\dot{n}_1 = \left(\frac{\gamma p}{1 + \sigma p} - \mu \right) n_1 + n_{1\,xx}, \tag{8}$$

$$\dot{w}_1 = (rp - p^2)n_1 - w_1 + \delta w_{1\,xx} - \delta \beta n_{1\,xx}. \tag{9}$$

Writing $(n_1, w_1) = (\hat{n}_1, \hat{w}_1)e^{st+ikx}$ we obtain the following expression from (8) which decouples from (9)

$$s = \left(\frac{\gamma p}{1 + \sigma p} - \mu \right) - k^2,$$

which shows that the bare state $\mathcal{B}$ undergoes an instability, at wavenumber $k = 0$, to vegetation when $\gamma p/(1 + \sigma p) = \mu$. Consideration of (9) shows that there are no other instabilities (the 2×2 linear system is lower triangular).

Re-arranging the condition for instability of $\mathcal{B}$ defines the critical rainfall parameter

$$p_c := \frac{\mu}{\gamma - \sigma \mu}. \tag{10}$$

The model construction implies the constraint $\gamma/\sigma > \mu$ that guarantees that for any level of soil water w, the rate of growth of vegetation at low biomass levels is greater than the rate μ at which biomass decays. The bifurcation at $p = p_c$ produces uniform vegetation states $\mathcal{V}$. From (6) we see that on $\mathcal{V}$ we must have $n = \gamma w/(1 + \sigma w) - \mu$. Substituting this into (7) we obtain the following cubic equation for w:

$$(\sigma \mu - \gamma)w^3 + (\mu + r(\gamma - \sigma \mu) - \sigma)w^2 + (p\sigma - 1 - r\mu)w + p = 0. \tag{11}$$

Solutions of (11) for which $w > 0$ correspond to physically admissible $\mathcal{V}$ solutions. The location of uniform states is shown in figure 1 and 2 which illustrate the dependence of the solution structure on the parameters r and γ respectively. All curves emerge from the horizontal axis at $p = p_c$, independent of r and δ. As r increases the cubic curve becomes steeper and then bistability emerges. The middle part of the solution branch in the bistable cases is unstable to uniform perturbations and is indicated by dashed lines. The dependence on γ is similar: as γ increases bistability develops. At sufficiently

4
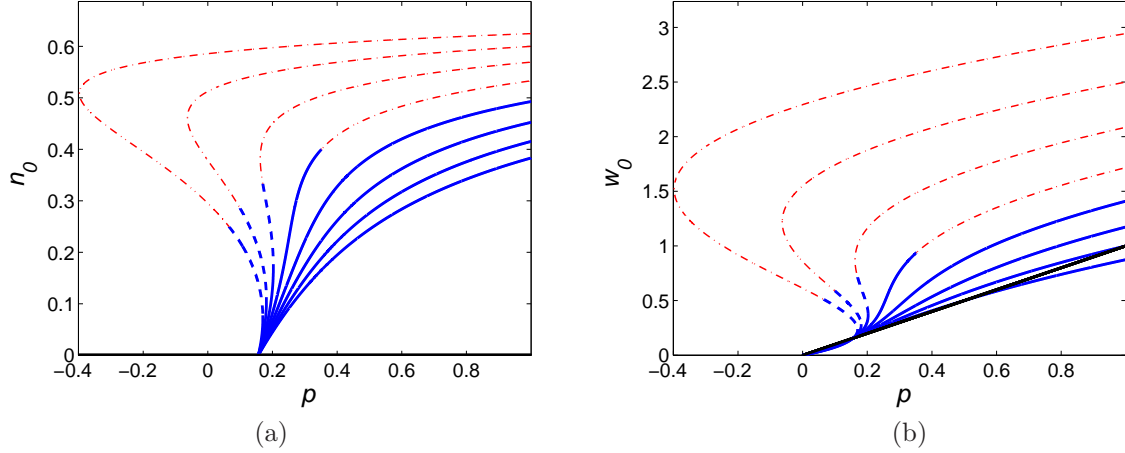
Figure 1: Bifurcation digrams showing the existence of $\mathcal{V}$ states and their stability: solid and dashed lines (blue) indicate stability and instability, respectively. Dashed-dotted lines (red) indicate unphysical solution branches where the shading factor $(1 - rn)$ has become negative. (a) in the (p, n) plane; (b) in the (p, w) plane. Bistability develops as r increases; the curves correspond to values $r = 0.5, 1, 1.5, 2, 2.5, 3, 3.5, 4$ from bottom to top. Other parameters: $\gamma = \sigma = 1.6$, $\mu = 0.2$.
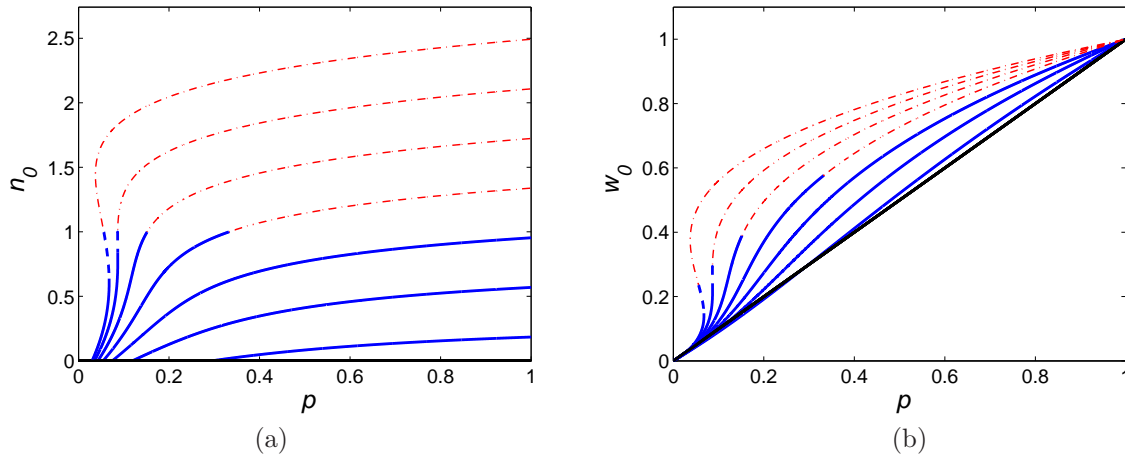
Figure 2: Bifurcation digrams showing the existence of $\mathcal{V}$ states and their stability: solid and dashed lines (blue) indicate stability and instability, respectively. Dashed-dotted lines (red) indicate unphysical solution branches where the shading factor $(1 - rn)$ has become negative. (a) in the (p, n) plane; (b) in the (p, w) plane. Bistability develops as γ increases; the four curves correspond to $\gamma = 1, 2, 3, 4, 5, 6, 7$ from bottom to top. Other parameters: $\sigma = 1.6$, $\mu = 0.2$, $r = 1.0$.

large values of either r or γ the saddle-node bifurcation point on the upper part of the uniform branch moves substantially to the left of $p = p_c$, i.e. the positive feedback effects parameterised by r and γ are sufficiently strong to sustain a uniform state in which significant vegetation and soil water are present even though the precipitation is well below the level required to sustain low levels of vegetation. Although these curves are smooth, as n_0 increases along a branch, the shading term $(1 - rn)$ decreases until it passes through zero. For $n > 1/r$, the term makes an unphysical contribution to the soil water level: the interpretation would have to be that the presence of biomass automatically introduced more water into the soil (i.e. a negative evaporation effect). The parts of the curves for which solutions remain physically relevant are indicated by the thicker blue lines. These include all the curves at small n_0, which indicates that this is a regime in which the model equations remain valid for all combinations of parameter values.

Despite the significant hysteresis exhibited by the solution branches, the bifurcation at $p = p_c$ is supercritical in all the cases shown in figures 1 and 2. for all parameter values, uniform states at small biomass exist in $p > p_c$. This can be justified straightforwardly since the slope of the curves $w(p)$, or

equivalently $p(w)$, shown in figure 1(b) and 2(b) can be computed explicitly as follows.

Differentiating (11) with respect to w we obtain

$$3(\sigma\mu - \gamma)w^2 + 2(\mu + r(\gamma - \sigma\mu) - \sigma)w + \frac{dp}{dw}(1 + \sigma w) + p\sigma - 1 - r\mu = 0.$$

We now set $w = p = p_c$ and re-arrange to obtain

$$\left.\frac{dp}{dw}\right|_{p_c} = 1 + \frac{\mu(p_c - r)}{1 + \sigma p_c}. \tag{12}$$

We are particularly interested in determining the range of parameter values for which $dp/dw|_{p_c}$ is positive, and hence $dw/dp|_{p_c}$ is positive, so that there is a small interval in the bifurcation parameter p, say $p_c < p < p_1$, above the initial bifurcation point, over which the $\mathcal{V}$ state is stable to uniform perturbations. In terms of the parameter r, these inequalities are satisfied when

$$r < p_c \left(1 + \frac{\gamma}{\mu^2}\right). \tag{13}$$

For the parameter values $\sigma = \gamma = 1.6$, $\mu = 0.2$ this evaluates to $r < 6.4062$ to 4 d.p. Alternatively, rearranging (12) to obtain a condition in terms of γ we find that $dw/dp|_{p_c}$ is positive when

$$\gamma(1 - r\mu) + \mu^2(1 + \sigma r) > 0.$$

For the parameter values $\sigma = 1.6$, $\mu = 0.2$ and $r = 1.0$, as used in figure 2, we observe that since $1 - r\mu > 0$, this condition holds for all γ.

2.2 Linear stability of $\mathcal{V}$

In addition to the saddle-node bifurcations shown in figures 1 and 2 there are additional possible pattern-forming instabilities in which $\mathcal{V}$ loses stability to spatially periodic perturbations. In this sub-section we summarise this linear stability calculation, which proceeds along well-known lines. Setting $(n, w) = (n_0, w_0) + (n_1(x, t), w_1(x, t))$ where n_0, w_0 is a uniform $\mathcal{V}$ solution, and linearising in the small perturbations (n_1, w_1), we obtain

$$\dot{n}_1 = \frac{\gamma(n_0 w_1 + w_0 n_1)}{1 + \sigma w_0} - \frac{\sigma\gamma w_0 n_0}{(1 + \sigma w_0)^2}w_1 - 2n_0 n_1 - \mu n_1 + n_{1\,xx}, \tag{14}$$

$$\dot{w}_1 = rw_0 n_1 - (1 - rn_0)w_1 - 2w_0 n_0 w_1 - w_0^2 n_1 + \delta(w_1 - \beta n_1)_{xx}. \tag{15}$$

To compute the response to spatially periodic perturbations, we write $(n_1, w_1) = (\hat{n}_1, \hat{w}_1)e^{st+ikx}$ and substitute this ansatz into (14) - (15). We obtain the following linear system involving a 2×2 matrix that we denote by M:

$$\begin{pmatrix} s - \frac{\gamma w_0}{1+\sigma w_0} + 2n_0 + \mu + k^2 & \frac{-\gamma n_0}{(1+\sigma w_0)^2} \\ -rw_0 + w_0^2 - \delta\beta k^2 & s + 1 - rn_0 + 2w_0 n_0 + \delta k^2 \end{pmatrix} \begin{pmatrix} \hat{n}_1 \\ \hat{w}_1 \end{pmatrix} = \begin{pmatrix} 0 \\ 0 \end{pmatrix}. \tag{16}$$

Non-zero solutions to this linear system exist only when $\det(M) = 0$. This condition then yields a quadratic expression for the growth rate s as a function of squared wavenumber k^2. Figure 3 illustrates these linear stability results, plotting the location of the $\mathcal{V}$ state in figure 3(a) and the least negative part of the growth rate curve in figure 3(b) which shows that the curve moves up above the $s = 0$ axis and then moves down below it as p is increased. The values of p at which the growth rate curve in (a) has a tangency with the $s = 0$ line correspond to the bifurcation points (solid dots) in (b) at which the lines change from solid to dashed, indicating instability. We label these bifurcation points as p_1 and p_2, using the convention that $p_c < p_1 < p_2$ (at least, for these parameter values). The parameters used in figure 3 correspond to those used in [9, figure 2] for ease of comparison.

In order to analyse the structure of these bifurcations in the weakly nonlinear regime we notice that the parameter δ naturally takes a value much larger than the other parameters. This is unavoidable since it represents the ratio of typical diffusion coefficients for soil water and vegetation: typical timescales for diffusion of soil water and vegetation are clearly extremly different; taking $\delta = 100$ seems perhaps to be an underestimate of the typical ratio of timescales we might expect. For comparison, the paper by Siteur et al [24] take the ratio of diffusion rates to be 500, see their parameter E in Appendix A and Table A.1.
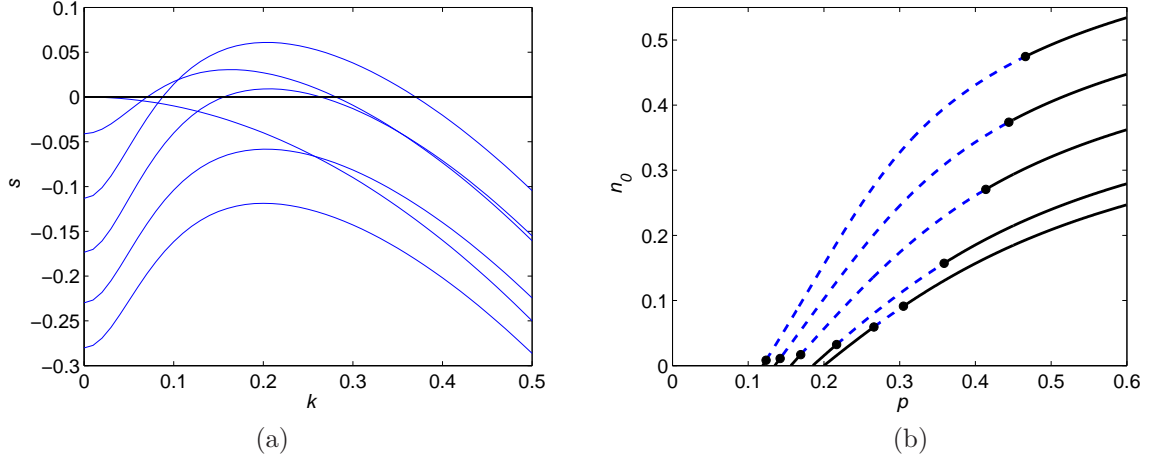
Figure 3: (a) Growth rate $s(k)$ for perturbations to the uniform vegetated state $\mathcal{V}$, as p increases above p_c. The curve lies below $s = 0$ near p_c and then moves above it before descending again at large p, indicating that the $\mathcal{V}$ state is stable at larger p. Parameters: $\gamma = \sigma = 1.6$, $\mu = 0.2$, $r = 1.5$, $\delta = 100$, $\beta = 3$. Growth rate curves are shown for $p \in \{p_c \equiv 0.15625, 0.2, 0.3, 0.4, 0.5, 0.6\}$: $s(0)$ decreases monotonically with increasing p. (b) Bifurcation digram in the (p, n_0) plane showing the existence of $\mathcal{V}$ states and their stability for $\gamma \in \{1.32, 1.4, 1.6, 1.8, 2.0\}$. Solid and dashed lines indicate stable and unstable solutions respectively, and black dots indicate pattern forming instabilities at points we refer to as p_1 and p_2, with the convention that $p_1 < p_2$. Other parameters are as in (a).
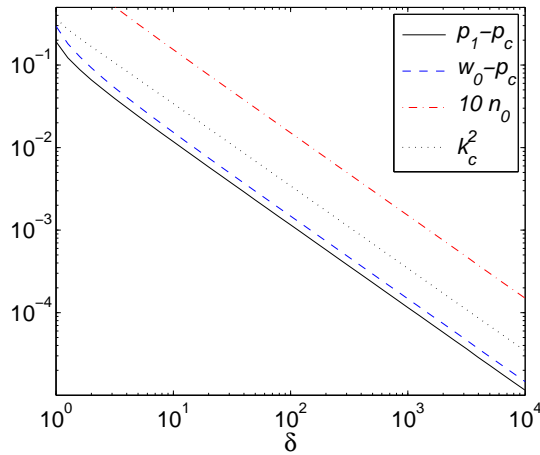
Figure 4: Scaling of quantities associated with p_1 as δ increases. Black line: the dependence of $p_1 - p_c$; blue dashed line: $w_0 - p_c$ where w_0 is evaluated at $p = p_1$ on $\mathcal{V}$; red dash-dotted line: n_0 evaluated at p_1 on $\mathcal{V}$ (shown scaled up by a factor of 10 for clarity); black dotted line: critical wavenumber k_c^2 at $p = p_1$.

Figure 4 indicates the movement of the bifurcation points and other quantities as δ increases while keeping all other parameters fixed. The figure indicates that these four quantities: $p_1 - p_c$, $w_0(p_1) - p_c$, $n_0(p_c)$ and k_c^2 all appear to scale $\sim 1/\delta$ as δ increases. These scalings therefore indicate that there might be a non-trivial limit of the model equations in the limit of large δ. Clearly large δ would also be expected to promote Turing-type instabilities since δ is a physically relevant ratio of diffusion coefficients; this might provide a useful simplifying route to aid the investigation of the dynamics of this model problem in ecologically relevant regimes.

If $p_1 - p_c$ is small then the pattern forming instability of $\mathcal{V}$ is close to the initial bifurcation of $\mathcal{V}$ from $\mathcal{B}$. We would therefore expect both the biomass n_0 and the change in soil water $w_0(p_1) - p_c$ to be small, of order $O(1/\delta)$ since at leading order they vary linearly with $p - p_c$. The fact that the pattern-forming instability involves a wavenumber $k \sim \delta^{-1/2}$ can be justified by examining the determinant of the matrix

M in (16), as follows. From (16) we have

$$\det(M) \equiv C(k^2) := \left[1 - rn_0 + 2w_0n_0 + \delta k^2\right] \left[-\frac{\gamma w_0}{1 + \sigma w_0} + 2n_0 + \mu + k^2\right], \tag{17}$$

so that a local maximum in $C(k^2)$ occurs when $dC/d(k^2) = 0$, i.e. when

$$C'(k^2) = 1 - rn_0 + 2w_0n_0 - \frac{\gamma \delta w_0}{1 + \sigma w_0} + 2\delta n_0 + \delta \mu + 2\delta k^2 - \frac{\gamma n_0 \delta \beta}{(1 + \sigma w_0)^2} = 0.$$

If we now set $n_0 = \hat{n}/\delta$ and $w_0 = p_c + \hat{w}/\delta$ then we obtain

$$2\delta k^2 = \frac{\gamma \beta \hat{n}}{(1 + \sigma p_c)^2} + \frac{\gamma \hat{w}}{1 + \sigma p_c} - \frac{\gamma p_c \sigma \hat{w}}{(1 + \sigma p_c)^2} - 1 - 2\hat{n} + O\left(1/\delta\right), \tag{18}$$

so that in the limit $\delta \gg 1$ we expect $k^2 \propto \delta^{-1}$ since the right-hand side of (18) is of order unity when $\hat{n}$ and $\hat{w}$ are of order unity.

2.3   Derivation of a reduced equation

In this subsection we use the observation made above, and the motivation from the numerical results shown in figure 4 to rescale the system (6) - (7) and simplify it to a single evolution equation for $n(x,t)$ in the limit of large δ.

We introduce the small parameter $\varepsilon := \delta^{-1}$ and write $p = p_c + \varepsilon P$, $n = \varepsilon N$ and $w = p + \varepsilon W$. Note that the threshold p_c for the instability of $\mathcal{B}$, and at which the $\mathcal{V}$ state emerges, is independent of δ. Given the scaling behaviour $k_c^2 \sim \delta^{-1}$ we also introduce the long lengthscale $X = \varepsilon^{1/2} x$, i.e. $\partial_x = \varepsilon^{1/2} \partial_X$. Note that this rescaled variable X is not related to the variables X, Y used earlier, in section 1.1.

Substituting these rescalings into (6) - (7) we obtain

$$\dot{N} = \frac{\gamma}{(1 + \sigma p_c)^2} \varepsilon P N - \varepsilon N^2 + \varepsilon N_{XX} + \frac{\gamma}{(1 + \sigma p_c)^2} \varepsilon W N + O(\varepsilon^2) \tag{19}$$

$$\dot{W} = -W + W_{XX} + (rp_c - p_c^2)N - \beta N_{XX} + O(\varepsilon). \tag{20}$$

These equations are not completely balanced since ε still appears in (19). This indicates that in the limit N evolves much more slowly in time than W. Consequently we may consider W to be rapidly determined by N through (20) which is, at leading order, linear. We therefore rescale time, setting $T = \varepsilon t$, and consider (20) to instantaneously determine W as a function of N. After rescaling time in this way, at leading order in ε there is no time derivative term in (20). Alternatively, we may formally solve the (now steady-state equation) (20) by defining the pseudodifferential operator $\mathcal{D}[N]$ by

$$W = (1 - \partial_X^2)^{-1}(rp_c - p_c^2 - \beta \partial_X^2)N =: \mathcal{D}[N]$$

or, in terms of spatial Fourier Transforms (where k is wavenumber corresponding to the spatial scale X):

$$\mathcal{F}[W](k) = \frac{rp_c - p_c^2 + \beta k^2}{1 + k^2} \mathcal{F}[N](k). \tag{21}$$

momentarily suppressing the dependence of W and N on T for notational convenience. Note that if $N(X, T) = N_0$ is constant, then $\mathcal{D}[N]$ just multiplies N by a constant: $\mathcal{D}[N_0] = (rp_c - p_c^2)N_0$. Similarly, high spatial wavenumber components of $N(X, T)$ will be scaled by a factor β. $\mathcal{D}$ is technically a pseudodifferential operator since its Fourier Transform is not a polynomial in k. In real-space it can be thought of as nonlocal convolution operator. More precisely, applying the convolution theorem for Fourier transforms to (21) we obtain

$$W(X, T) = \beta N(X, T) + (rp_c - p_c^2 - \beta) \int_{-\infty}^{\infty} e^{-|X-Y|} N(Y, T) \, dY. \tag{22}$$

After including the time rescaling $T = \varepsilon t$ we conclude that, asymptotically in the limit of large δ the dynamics of the von Hardenberg model for small vegetation levels $0 < n(x, t) \ll 1$ should be well captured by the single equation

$$N_T = b_0 P N - N^2 + N_{XX} + b_0 N \mathcal{D}[N], \tag{23}$$

8

or equivalently the elliptic-parabolic system

$$N_T = b_0 PN - N^2 + N_{XX} + b_0 WN, \qquad (24)$$

$$0 = W_{XX} - W + (rp_c - p_c^2)N - \beta N_{XX}, \qquad (25)$$

where $b_0 = \gamma/(1 + \sigma p_c)^2$ and $p_c = \mu/(\gamma - \sigma\mu)$ are positive coefficients. Given the range of δ over which the scalings appear in figure 4, in fact δ might not need to be particularly large for this reduced system to provide useful insight into the dynamics of the von Hardenberg et al model.

3   Dynamics of the reduced model

Having derived the reduced model (23) in the previous section, in this section we summarise its dynamics; the weakly nonlinear analysis that determines the pattern forming behaviour of (6) - (7) for low levels of vegetation can be carried out and presented completely, although it does lead to coefficients that have a reasonably complicated dependence on the underlying problem parameters. However, this can be illustrated graphically and allows us in particular to elucidate the role of the feedback parameter r.

The reduced model in the form (23) clearly has two uniform, constant states: $N \equiv 0$ (corresponding to the bare state $\mathcal{B}$) and the uniform vegetation state $\mathcal{V}$ for which $N = N_0 > 0$ where N_0 is defined to be

$$N_0 = \frac{\gamma P}{(1 + \sigma p_c)^2 - \gamma(rp_c - p_c^2)}. \qquad (26)$$

For later convenience we define the combination of coefficients on the right-hand side to be a new parameter b_1, hence we write the $\mathcal{V}$ state as $N_0 = b_1 P$.

Recall that $P \propto p - p_c$ is the scaled precipitation parameter, so that in the reduced model the level of vegetation increases linearly with the rainfall parameter P, and that the $\mathcal{V}$ solution exists in $P > 0$ as long as r is small enough. More precisely, the bifurcation is supercritical for $r < r_*$ and subcritical for $r > r_*$ where

$$r_* := p_c + \frac{(1 + \sigma p_c)^2}{\gamma p_c} = \frac{\mu^2 + \gamma}{\mu(\gamma - \sigma\mu)} = p_c\left(1 + \frac{\gamma}{\mu^2}\right),$$

which agrees with the inequality in (13). For stable patterns to form we are naturally more interested in the regime $r < r_*$.

3.1   Linear and weakly nonlinear analysis

In terms of the formulation (24) - (25), the $\mathcal{B}$ and $\mathcal{V}$ states correspond to $N = W = 0$ and $N = N_0$, $W = W_0 = (rp_c - p_c^2)N_0$. To examine linear instabilities of the $\mathcal{V}$ state, we first set $N = N_0 + U(X, T)$ and $W = W_0 + V(X, T)$ and substitute these expressions into (24) - (25). This results in the system

$$U_T = -b_1 P + U_{XX} - U^2 + b_0 b_1 PV + b_0 UV. \qquad (27)$$

$$V - V_{XX} = (rp_c - p_c^2)U - \beta U_{XX} \qquad (28)$$

Linearising around the state $U = V = 0$ we deduce that this solution becomes linearly unstable to perturbations $\sim e^{ik_c X}$ when

$$P^2(b_0 b_1 \beta - b_1)^2 + 2P[b_2 + 2b_0 b_1(rp_c - p_c^2 - \beta/2)] + 1 = 0$$

and so $\mathcal{V}$ loses stability first when

$$P = P_0 := \frac{-[2b_0 b_1(rp_c - p_c^2 - \beta/2) - b_1] + [[2b_0 b_1(rp_c - p_c^2 - \beta/2) - b_1]^2 - (b_0 b_1 \beta - b_1)^2]^{1/2}}{(b_0 b_1 \beta - b_1)^2}. \qquad (29)$$

The critical wavenumber of this instability is k_c, where

$$k_c^2 = \frac{1}{2}(P_0(b_0 b_1 \beta - b_1) - 1). \qquad (30)$$

This is therefore a pattern-forming instability whose weakly nonlinear development can be analysed using a standard multiple-scales approach as we now describe.

Propose the expansion

$$
\begin{aligned}
U &= \varepsilon U_1 + \varepsilon^2 U_2 + \varepsilon^3 U_3 + \cdots \\
V &= \varepsilon V_1 + \varepsilon^2 V_2 + \varepsilon^3 V_3 + \cdots
\end{aligned}
$$

where we set $U_1 = A e^{ik_c X} + c.c.$ and the amplitude $A(\xi, \tau)$ is a function of the new rescaled long space and time variables $\xi = \varepsilon X$ and $\tau = \varepsilon^2 T$ respectively, and $c.c.$ denotes the complex conjugate of the immediately preceding term. In addition let $P = P_0 + \varepsilon^2 \mu$. Considering (28) at $O(\varepsilon)$ we find that

$$
V_1 = \frac{rp_c - p_c^2 + \beta k_c^2}{1 + k_c^2}(A e^{ik_c X} + c.c.).
$$

Turning to $O(\varepsilon^2)$ terms, we see that (28) yields

$$
V_2 - V_{2XX} - 2V_{1X\xi} = (rp_c - p_c^2)U_2 - \beta U_{2XX} - 2\beta U_{1X\xi}.
$$

We observe that the quadratic interactions in (28) will imply that U_2 takes the form $U_2 = B(\xi, \tau)e^{2ik_c X} + c.c. + C(\xi, \tau)$, where the amplitudes $B(\xi, \tau)$ and $C(\xi, \tau)$ are amplitudes of the modes with wavenumbers $2k_c$ and 0, respectively. Given this form for U_2 we can then deduce that

$$
\begin{aligned}
V_2 &= 2ik_c \left[\frac{rp_c - p_c^2 + \beta k_c^2}{(1 + k_c^2)^2} - \frac{\beta}{1 + k_c^2}\right](A_\xi e^{ik_c X} - \bar{A}_\xi e^{-ik_c X}) + (rp_c - p_c^2)C \\
&\quad + \frac{rp_c - p_c^2 + 4\beta k_c^2}{1 + 4k_c^2}(B e^{2ik_c X} + c.c.).
\end{aligned}
\tag{31}
$$

Now we consider equation (27) at $O(\varepsilon^2)$, which gives

$$
0 = -U_2 b_1 P_0 + b_0 b_1 P_0 V_2 + U_{2XX} + 2U_{1X\xi} - U_1^2 + b_0 U_1 V_1.
\tag{32}
$$

Then, substituting (31) into (32) enables us to solve for $B(\xi, \tau)$ and $C(\xi, \tau)$ in terms of $A(\xi, \tau)$. We find that

$$
B = b_3 A^2, \qquad \text{and} \qquad C = b_4 |A|^2,
\tag{33}
$$

where the coefficients are

$$
\begin{aligned}
b_3 &:= \frac{1 - b_0(rp_c - p_c^2 + \beta k_c^2)/(1 + k_c^2)}{(b_0 b_1 P_0(rp_c - p_c^2 + 4\beta k_c^2))/(1 + 4k_c^2) - P_0 b_1 - 4k_c^2} \\
b_4 &:= 2\frac{1 - b_0(rp_c - p_c^2 + \beta k_c^2)/(1 + k_c^2)}{-b_0 P_0}.
\end{aligned}
$$

The terms involving iA_ξ and $i\bar{A}_\xi$ in (32) vanish identically (and correctly) through our choice of P_0 as a root of the quadratic expression (29) and our corresponding selection of the critical wavenumber k_c.

Considering terms at $O(\varepsilon^3)$ in (28) and (27), we need to solve

$$
\begin{aligned}
V_3 - V_{3XX} - 2V_{2X\xi} - V_{1\xi\xi} &= (rp_c - p_c^2)U_3 - \beta U_{3XX} - 2\beta U_{2X\xi} - \beta U_{1\xi\xi}, \tag{34} \\
U_{1\tau} + U_{3T} &= -b_1(U_3 P_0 + U_1 \mu) + b_0 b_1 P_0 V_3 + b_0 b_1 \mu V_1 + U_{3XX} \\
&\quad + 2U_{2X\xi} + U_{1\xi\xi} - 2U_1 U_2 + b_0 U_1 V_2 + b_0 U_2 V_1. \tag{35}
\end{aligned}
$$

From (34) we observe that V_3 contains terms $\sim e^{ik_c X}$ that (generically) will result in a resonant response:

$$
V_3 - V_{3XX} = \left[-4k_c^2\left(\frac{rp_c - p_c^2 + \beta k_c^2}{(1 + k_c^2)^2} - \frac{\beta}{1 + k_c^2}\right) + \frac{rp_c - p_c^2 + \beta k_c^2}{1 + k_c^2} - \beta\right]A_{\xi\xi}e^{ik_c X} + c.c. + NRT
$$

where NRT stands for 'non-resonant terms', i.e. those terms that have a Fourier dependence on the shorter lengthscale X of the form $e^{imk_c X}$ with $m \in \mathbb{Z}\backslash\{1, -1\}$. Hence the resonant part of V_3 takes the form $V_3^{(1)} + c.c.$ where

$$
V_3^{(1)} = \frac{1}{1 + k_c^2}\left\{-4k_c^2\left(\frac{rp_c - p_c^2 + \beta k_c^2}{(1 + k_c^2)^2} - \frac{\beta}{1 + k_c^2}\right) + \frac{rp_c - p_c^2 + \beta k_c^2}{1 + k_c^2} - \beta\right\}A_{\xi\xi}e^{ik_c X}.
$$

So, when we return to (35) we see that the resonant terms of the form e^{ik_cX} indicate that the amplitude equation for $A(\xi,\tau)$ takes the form

$$
\begin{aligned}
A_\tau =\ & -b_1\mu A + \mu A b_0 b_1 \left(\frac{rp_c - p_c^2 + \beta k_c^2}{1 + k_c^2} \right) + A_{\xi\xi} \\
& -2(AC + B\bar{A}) + b_0(rp_c - p_c^2)AC + b_0 \left(\frac{rp_c - p_c^2 + 4\beta k_c^2}{1 + 4k_c^2} \right) B\bar{A} \\
& + b_0 \frac{rp_c - p_c^2 + \beta k_c^2}{1 + k_c^2}(B\bar{A} + AC) + V_3^{(1)}
\end{aligned}
$$

where $B(\xi,\tau)$ and $C(\xi,\tau)$ are given in (33). Hence, simplifying, this is (as must be the case on symmetry grounds) a standard cubic Ginzburg–Landau equation taking the form

$$
A_\tau = \mathcal{C}_1\mu A + \mathcal{C}_2 A_{\xi\xi} + \mathcal{C}_3 A|A|^2 \tag{36}
$$

where the coefficients are given explicitly as follows.

$$
\begin{aligned}
\mathcal{C}_1 =\ & -b_1 + b_0 b_1 \left(\frac{rp_c - p_c^2 + \beta k_c^2}{1 + k_c^2} \right), \\
\mathcal{C}_2 =\ & 1 + \frac{b_0 b_1 P_0}{1 + k_c^2} \left\{ -4k_c^2 \left(\frac{rp_c - p_c^2 + \beta k_c^2}{(1 + k_c^2)^2} - \frac{\beta}{1 + k_c^2} \right) + \frac{rp_c - p_c^2 + \beta k_c^2}{1 + k_c^2} - \beta \right\}, \\
\mathcal{C}_3 =\ & -2(b_3 + b_4) + b_0 b_4(rp_c - p_c^2) + b_0 b_3 \frac{(rp_c - p_c^2 + 4\beta k_c^2)}{1 + 4k_c^2} + b_0(b_3 + b_4)\frac{rp_c - p_c^2 + \beta k_c^2}{1 + k_c^2}.
\end{aligned}
$$

3.2   Results of the weakly nonlinear analysis

In this subsection we summarise the dependencies of the coefficients $\mathcal{C}_1, \ldots \mathcal{C}_3$ on the original problem parameters, for the rescaled equations (24) - (25). As discussed previously we keep μ and σ fixed and vary the feedback parameters γ, r and β. Figure 5 shows four surface plots for the quantities $\mathcal{C}_1$, k_c, $\mathcal{C}_2$ and $\mathcal{C}_3$ as functions of γ and r for fixed $\beta = 3.0$.

We observe that a pattern forming instability exists only for γ sufficiently large: $\gamma > \gamma_c \approx 0.85$ in figure 5. Figure 5(b) indicates that as γ decreases towards γ_c the critical wavenumber k_c diverges to infinity. An analytic expression for γ_c is given implicitly by setting the expression (30) equal to zero. $\mathcal{C}_1$ and $\mathcal{C}_2$ remain positive for all $\gamma > \gamma_c$ and r indicating that the weakly nonlinear amplitude equation is always well-posed. The dependence of these coefficients on r appears to be quite weak compared to their dependence on γ. Figure 5(d) shows that for γ just above γ_c the coefficient $\mathcal{C}_3$ is negative in a region bounded by the line $\gamma = \gamma_c$ and the black sloping line shown in figure 5(d); the pattern-forming instability is therefore supercritical in this region. To the right of this sloping line $\mathcal{C}_3$ is positive indicating that the instability is now subcritical. The sloping line therefore describes the location of higher-codimension (sometimes referred to as 'tricritical' points) at which higher-order terms are necessary in order to determine the bifurcation behaviour.

Figure 6 shows the values of $\mathcal{C}_1$, $\mathcal{C}_2$ (rescaled by a factor of 10) and $\mathcal{C}_3$ as γ is varied, keeping $r = 1.5$ constant. This illustrates in more detail that the supercritical region, in which $\mathcal{C}_3 < 0$, occurs only near $\gamma = \gamma_c$ and $\mathcal{C}_3$ is positive and increases rapidly as γ increases away from γ_c.

Figure 7 illustrates the dependence of the coefficients at fixed $r = 1.5$. The pattern forming instability does not occur if either γ or β is sufficiently small: as in figure 5(b), figure 7(b) shows that k_c increases rapidly as this lower limit is approached. In order to survey a greater range of parameter values, in figure 7 the contours are shown on a log–log scale, and moreover the colour scale corresponds to the logarithm of the coefficients. Figure 7(d) again illustrates that for values of γ and β near the lower boundary of the pattern forming region, $\mathcal{C}_3 < 0$ in a strip, shown in dark blue, between two solid black curves. Therefore the instability is persistently supercritical near this lower boundary before becoming subcritical at larger values of either γ or β.

It appears, from figure 7, that in the limit of large γ the coefficients $\mathcal{C}_1, \ldots, \mathcal{C}_3$ appear to depend on β and γ, as a good approximation, through the product $\beta\gamma$; the coefficients are almost constant on lines with slope -1 in these log–log plots. This observation can be justified by observing that the rescaling

$$
P = \frac{1}{\gamma}\hat{P}, \qquad W = \frac{1}{\gamma}\hat{W}, \qquad \beta = \frac{1}{\gamma}\hat{\beta}
$$
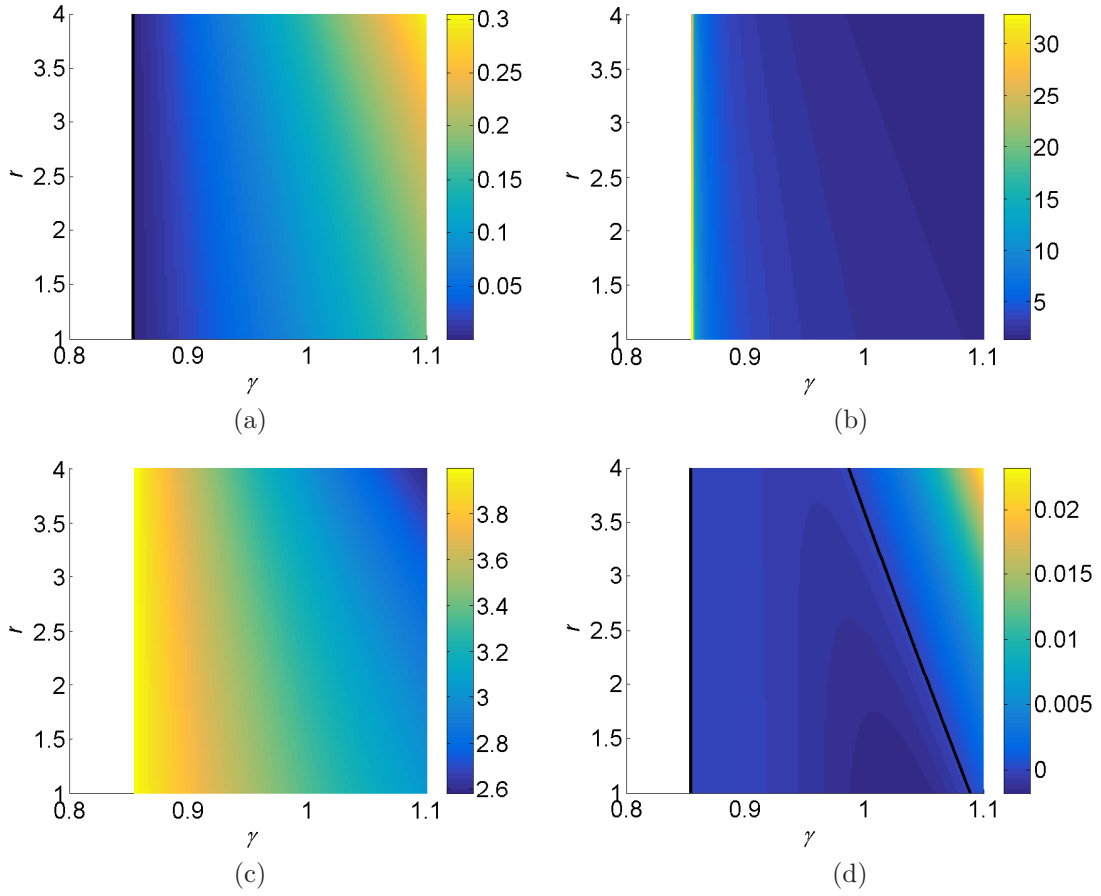
Figure 5: Surface plots in the (γ, r) plane. (a) $\mathcal{C}_1$; (b) k_c; (c) $\mathcal{C}_2$; (d) $\mathcal{C}_3$. Other parameters are held fixed at $\beta = 3.0$, $\mu = 0.2$, $\sigma = 1.6$. The black line in (d) is a curve on which $\mathcal{C}_3 = 0$.
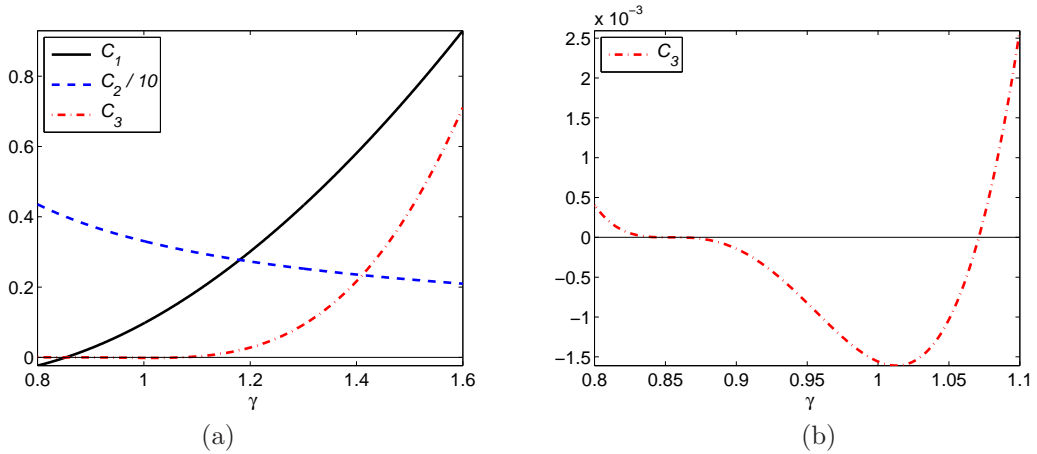
Figure 6: Coefficients $\mathcal{C}_1, \mathcal{C}_2, \mathcal{C}_3$ as functions of γ. Note that $\mathcal{C}_2$ is rescaled by a factor of 10. (b) is an enlargement of (a) showing that $\mathcal{C}_3$ is negative over a small interval in γ. Other parameters are held fixed at $\beta = 3.0$, $\mu = 0.2$, $\sigma = 1.6$, $r = 1.5$.
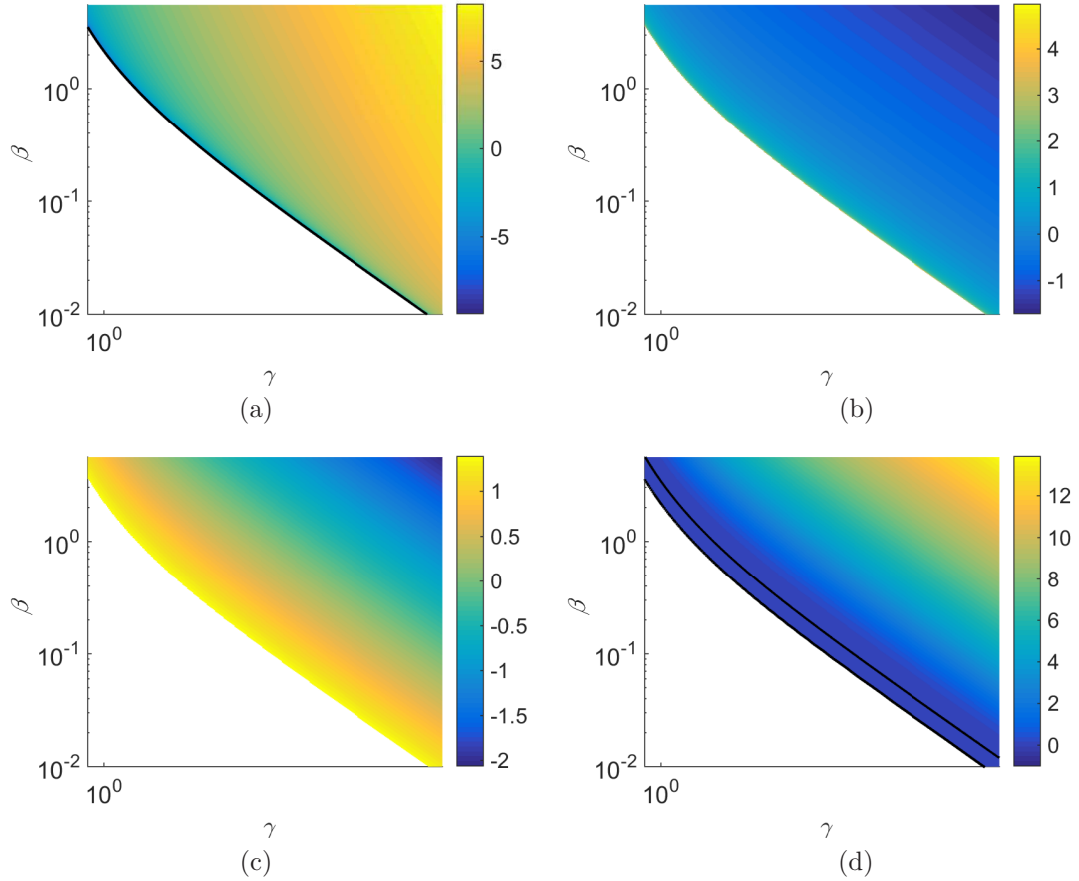
Figure 7: Surface plots of the coefficients $\mathcal{C}_1, \dots \mathcal{C}_3$ and k_c in the (γ, β) plane. As these quantities vary rapidly with γ and β the precise quantities diplayed are (a) $\log \mathcal{C}_1$; (b) $\log k_c$; (c) $\log \mathcal{C}_2$; (d) $\log(1+\mathcal{C}_3)$. Other parameters are held fixed at $r = 1.5$, $\mu = 0.2$, $\sigma = 1.6$. Solid lines in (a) and (d) correspond to zero contours. Note that $\mathcal{C}_3 < 0$ in a thin strip between the solid black lines. In the lower-left white region of each plot there is no pattern-forming instability and the coefficients in the amplitude equation are undefined.
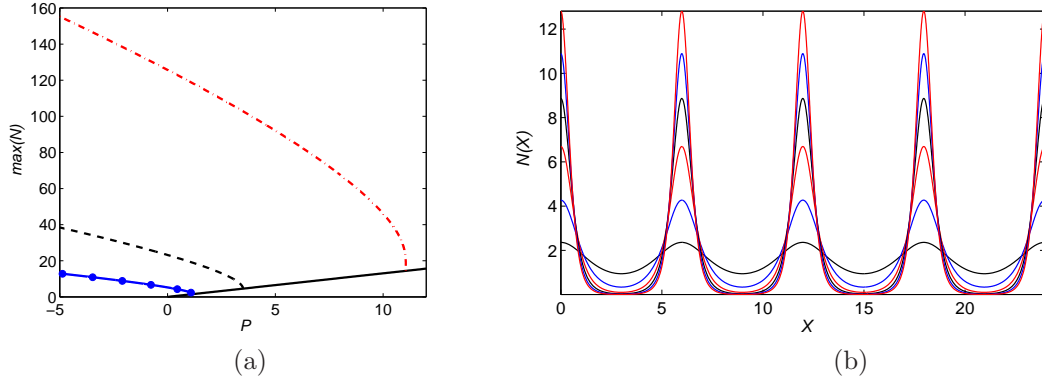
Figure 8: (a) Bifurcation diagram in the $(P, \max(N))$ plane showing branches of periodic patterns that bifurcate from the $\mathcal{V}$ solution at $P = P_0$. The location of P_0 increases as β decreases: bifurcating solution branches are shown for $\beta = 3$ (solid blue line), $\beta = 2$ (dashed black line) and $\beta = 1.5$ (dash-dotted red line). (b) Solution profiles $N(X)$ along the $\beta = 3$ branch at the six points indicated by solid dots in (a). The amplitude of the pattern increases monotonically as P decreases. Other parameter values are: $r = 1.5$, $\gamma = 1.6$, $\mu = 0.2$ and $\sigma = 1.6$.

and taking the limit $\gamma \gg 1$, transforms (24) - (25) into

$$N_T = PN - N^2 + N_{XX} + WN \tag{37}$$
$$W - W_{XX} = r\mu N - \hat{\beta} N_{XX} \tag{38}$$

dropping the hats on P and W, and noting that $p_c = \mu/\gamma + O(\gamma^{-2})$ and $b_0 = \gamma + O(1)$ in the limit of large γ. This rescaled model preserves the pattern-forming behaviour of (24) - (25); for example (37) - (38) has constant solutions $\mathcal{B}$, for which $N = W = 0$, and $\mathcal{V}$, for which $N = P/(1 - r\mu)$ and $W = r\mu P/(1 - r\mu)$. As we would expect, this $\mathcal{V}$ solution agrees with the limiting behaviour of (26) applying the rescalings noted above in the limit $\gamma \ll 1$.

We conclude that, as long as k_c given by (30) is positive, we have a non-degenerate pattern forming instability for values of the precipitation parameter just above p_c. There is a bounded region in parameter space for which this instability is supercritical, and it is subcritical more generally. An increase in any of the three parameters β, γ and r that describe 'positive feedback' physical effects in the model, leads to this instability becoming ever more strongly subcritical.

3.3 Dynamics at larger amplitude

In the previous subsection we examined the onset of pattern forming behaviour and showed that periodic patterns bifurcated subcritically except in a narrow region of parameter space where the product $\beta\gamma$ is sufficiently small. For the reduced model (24) - (25), numerical continuation of periodic patterns shows that they extend over considerable distances into $P < P_0$ and acquire an extremely sharp peaked profile.

Figures 8 and 9 show curves of periodic patterns with wavenumber exactly k_c that bifurcate from the uniform $\mathcal{V}$ solution at $P = P_0$, for three different values of β. For the lowest of these values, $\beta = 1.5$, the solution bifurcates supercritically before turning around. For larger values of β the patterned branches bifurcate subcritically. In all cases the branches appear to extend monotonically to arbitrarily large negative P.

The $\mathcal{V}$ solution is the straight line at the bottom of figure 8(a). For $\beta = 3$ the patterned branch bifurcates at $P \equiv P_0 = 1.185$. For $\beta = 2$ and $\beta = 1.5$ we find that $P_0 = 3.502$ and $P_0 = 11.054$, respectively. In each case the solutions are computed on a domain of width equal to the periodicity of the solution at the bifurcation point. The wavenumbers for the cases $\beta = 3, 2, 1.5$ are $k_c = 1.050, 1.376$ and 1.834 respectively.

Figure 9 plots the same bifurcation diagram as in figure 8 showing that the amplitude of $W(X)$ increases similarly to $N(X)$. Figure 9(b) shows the form of the periodic patterns at the points indicated on the lowest branch of periodic solutions, for $\beta = 3$, indicated by the solid dots in figure 9(a). The initially sinsoidal pattern evolves to contain sharp peaks separated by regions in which $W(X) < 0$, with local minima in $W(X)$ either side of each peak and a local maximum symmetrically placed between each pair of peaks. Physically this corresponds to the occurrence of a very dry barren patch between vegetated tufts, but with the centre of each barren patch being slightly less dry than the immediate

14
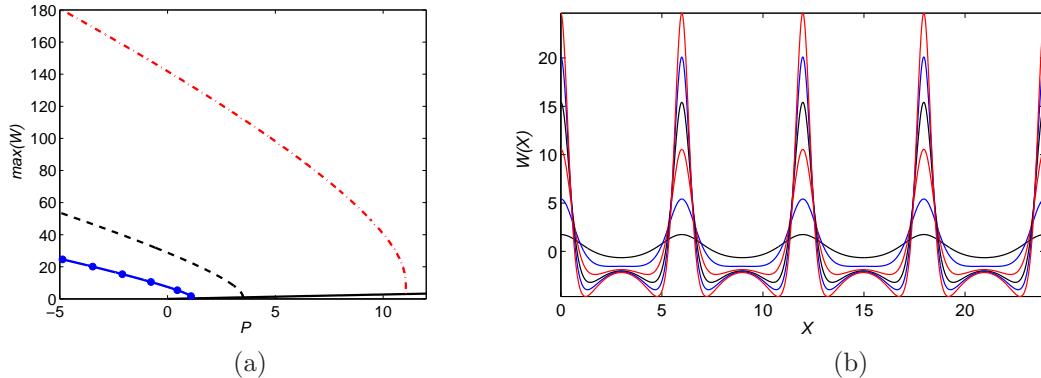
Figure 9: (a) Bifurcation diagram in the $(P, \max(W))$ plane showing branches of periodic patterns that bifurcate from the $\mathcal{V}$ solution at $P = P_0$. The location of P_0 increases as β decreases: bifurcating solution branches are shown for $\beta = 3$ (solid blue line), $\beta = 2$ (dashed black line) and $\beta = 1.5$ (dash-dotted red line). (b) Solution profiles $W(X)$ along the $\beta = 3$ branch at the six points indicated by solid dots in (a). The amplitude of the pattern increases monotonically as P decreases. Other parameter values are: $r = 1.5$, $\gamma = 1.6$, $\mu = 0.2$ and $\sigma = 1.6$.

vicinity of the tufts themselves; this might seem slightly counterintuitive, but indicates that the feedback between biomass and soil water is sufficiently strong that the biomass extracts water from the soil around it more strongly than water is able to smooth out the resulting gradient in water concentration through diffusion.

4   Localised patterns in the von Hardenberg model

In the previous section we established that the pattern forming instability that arises in the reduced model (24) - (25) at $P = P_0$ is subcritical as long as $\beta\gamma$ is sufficiently large. From bifurcation theory, and detailed investigation of the canonical Swift–Hohenberg equation, it is well known that in addition to branches of spatially periodic patterns, branches of spatially localised states can emerge from the bifurcation point.

In the usual case, at least in one spatial dimension, these branches of localised states form a structure known as 'homoclinic snaking' in a region between the initial bifurcation point and the saddle-node that marks the lower bound to the region over which the subcritical spatially periodic patterns exist. For details of typical homoclinic snaking behaviour see [2, 5, 3] and references therein.

Homoclinic snaking has been most widely studied in the canonical model equation: the 1D Swift–Hohenberg equation

$$\partial_t u = \left[r - (1 + \partial_x^2)^2 \right] u + bu^2 - u^3, \tag{39}$$

for a scalar variable $u(x, t)$, where r and b are real parameters. In (39) the base state $u(x, t) \equiv 0$ undergoes a pattern-forming instability as r passes through zero, i.e. perturbations with wavenumber 1 destabilise the base state at this parameter value. Analysis shows that when $b^2 < \frac{27}{38}$ the Turing instability at $r = 0$ is supercritical and small amplitude stable patterns exist in $r > 0$. In the weakly nonlinear regime, stable periodic patterns are possible as long as the pattern wavenumber k remains within an interval around $k = 1$.

If $b^2 > \frac{27}{38}$ then the Turing instability at $r = 0$ is subcritical and there are no stable small amplitude periodic patterns. The cubic term indicates that stable patterns exist at finite amplitude and increasing r past $r = 0$ indicates a jump onto one of these stable solution branches in $r > 0$. Moreover, in the subcritical case a pair of branches of spatially modulated near-periodic solutions bifurcate into $r < 0$ along with the small-amplitude unstable exactly periodic branches. Along this pair of spatially modulated solution branches the solutions become increasingly spatially localised, as indicated in figures 10 and 11. At some point in $r < 0$ the branches begin to oscillate backwards and forwards across an interval in r: these successive twists and turns correspond to saddle-node bifurcations and as we continue along each curve new peaks are added to the localised structure until, in a finite domain, the solution fills the domain and then becomes spatially periodic again. At this point, at the top of the snake in a finite
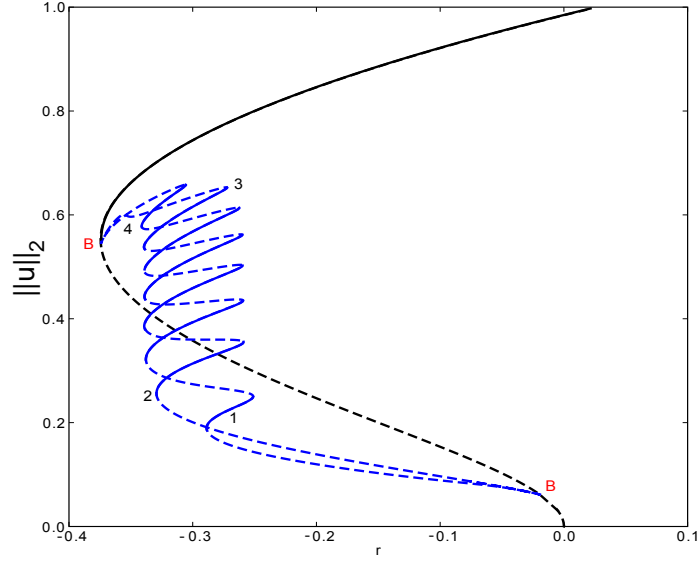
Figure 10: Homoclinic snaking for the Swift–Hohenberg equation: bifurcation diagram showing branches of periodic patterns (black) and localised states (blue) in the $(r, ||u||_2)$-plane for the quadratic-cubic SHE (39), for $b = 1.8$. Solid (dashed) lines indicate stable (unstable) solutions. Points marked 'B' are the bifurcations at which the localised states emerge from the periodic states and are a consequence of the finite computational domain. The computational domain was $0 \leq x \leq 20\pi$, with periodic boundary conditions. This figure was computed using the continuation software AUTO [6].
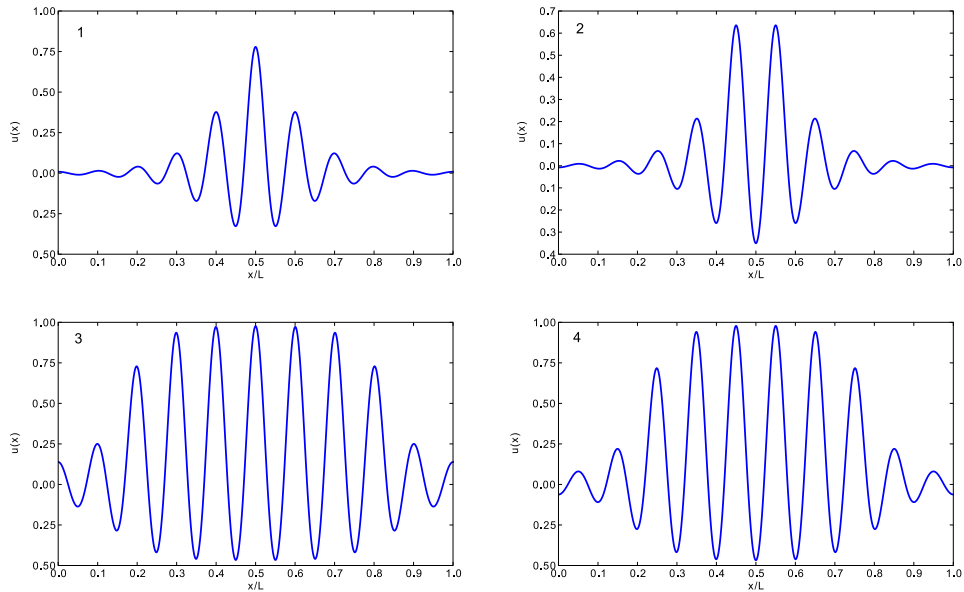
Figure 11: Homoclinic snaking for the Swift–Hohenberg equation: illustrative solution profiles $u(x, t)$ at the four numbered locations $1, 2, 3, 4$ on the bifurcation diagram in figure 10. The computational domain was $0 \leq x \leq 20\pi$, with periodic boundary conditions. As in the case of figure 10, the computations were carried out using the continuation software AUTO [6].

domain, these snaking branches reconnect to periodic pattern branches that bifurcate from (close to) $r = 0$. This bifurcation structure occurs generically near a subcritical Turing instability, and so we expect to observe it near p_1 (and p_2) when these pattern forming bifurcations are subcritical. Various
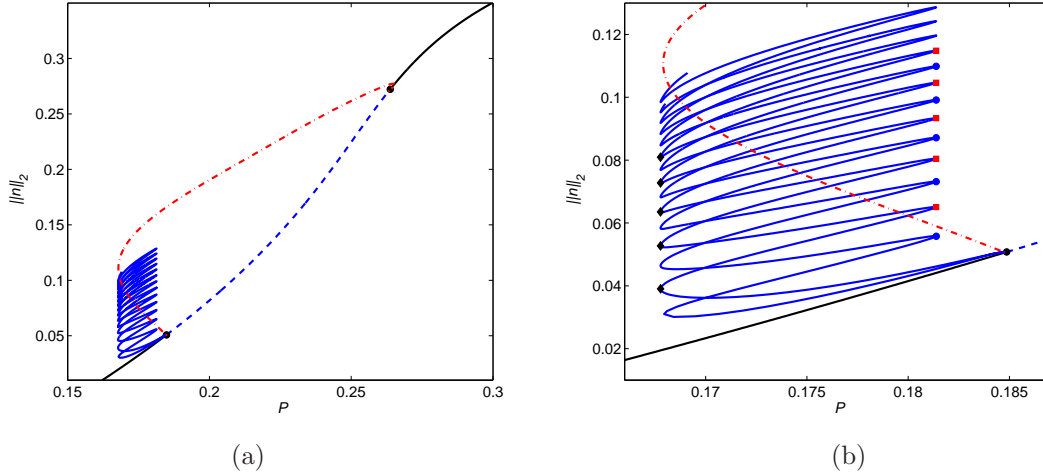
Figure 12: (a) Bifurcation diagram for the unscaled von Hardenberg model (6) - (7) shown in the $(p, ||n||)$ plane. Parameter values are $\gamma = \sigma = 1.6$, $\mu = 0.2$, $r = 2.5$, $\delta = 30$. Domain size $L = 400$, using periodic boundary conditions. (b) Enlargement of (a) showing the snaking region. The solid (black) curve and the dashed (blue) indicate the uniform $\mathcal{V}$ solution (stable and unstable, respectively). The periodic pattern branch is indicated by the dash-dotted (red) curve: stability is not indicated on this branch. The solid (blue) curves close together are the homoclinic snaking curves on which localised states lie; stability is not indicated on these branches. Dot, square and diamond symbols relate to solutions shown in figures 13 and 14.

details of the homoclinic snaking depend on the choice of nonlinear terms in the system, so it is possible that the bifurcation structure, and the stability of the localised states, varies from one specific nonlinear problem to another.

We now turn back to the specific model (6) - (7) and present numerical evidence for the existence of localised patterns near p_1. Figure 12 illustrates that this homoclinic snaking bifurcation behaviour occurs in the von Hardenberg model: figure 12(a) shows the $\mathcal{V}$ solution which is stable at sufficiently small and sufficiently large p, together with the bifurcating branch of periodic pattern (the red dash-dotted curve) that has the wavenumber at the onset of the pattern-forming instability. Although stability of these periodic patterns is not shown, the branch is unstable near $\mathcal{V}$ since the bifurcation is subcritical. The periodic pattern re-stabilises at the saddle-node bifurcation on the curve and is then stable until it reconnects to the $\mathcal{V}$ solution at larger p. As is generic for subcritical pattern forming instabilities of this type, we find also that a collection of localised states also bifurcates at the pattern forming instability. The homoclinic snaking curves are shown more clearly in the enlargement in figure 12(b). There are two distinct branches of solutions: both are symmetric under $x \to -x$. The branches consist of solutions that have local minima, or local maxima, at the centre, respectively. The branches do not intersect except where both bifurcate from $\mathcal{V}$. General theoretical resuts imply the existence of additional, asymmetric and typically unstable, solutions that connect between the two primary snaking branches, bifurcating in subcritical pitchfork bifurcations.

The snaking curves oscillate back and forth in p as additional peaks are added to the edges of the localised state. In a finite domain with Neumann boundary conditions the snaking curves typically terminate at a bifurcation point on a branch of spatially periodic solutions, although this need not be the one that bifurcated at the initial linear instability of $\mathcal{V}$ at p_c. In figure 12 we have not continued the branches as far as this point. Figure 12 indicates also that the snaking region extends slighly below the saddle-node bifurcation point on the periodic pattern branch shown. This indicates that the periodic pattern that bifurcates at the linear instability at p_c does not have exactly the same wavenumber as the periodic pattern within the localised state. This is generically the case, although in the Swift–Hohenberg equation with the usual nonlinearities the wavenumber selected by the localised patch is close (and with the cubic-quintic nonlinearity, very close) to that of the periodic pattern formed at p_c.

The equilibrium solutions $n(x)$ at the solid blue dots, red squares and black diamonds at saddle node points in figure 12 are shown in figure 13 and 14. More precisely, figure 13(a) shows $n(x)$ at the lowest five saddle-node bifurcation points on the 'odd-peak' branch of snaking, and figure 13(b) shows $n(x)$ at the lowest five saddle-node bifurcation points on the 'even-peak' branch. Note that the amplitude of the peaks is significantly higher than the constant $\mathcal{V}$ solution that surrounds the localised patch.
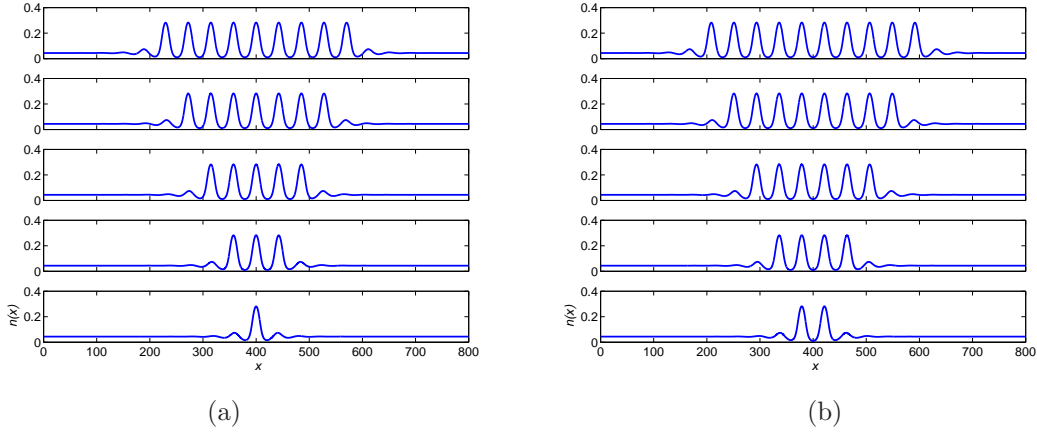
Figure 13: Localised equilibrium solutions $n(x)$ for the von Hardenberg model (6) - (7). The solution for $n(x)$ is shown, for parameter values $\gamma = \sigma = 1.6$, $\mu = 0.2$, $r = 2.5$, $\delta = 30$. Computed in a domain of size $L = 400$, using Neumann boundary conditions. (a) Solutions with odd numbers of peaks at the points indicated by the blue circles in figure 12(b). (b) Solutions with even numbers of peaks at the points indicated by the red squares in figure 12(b).
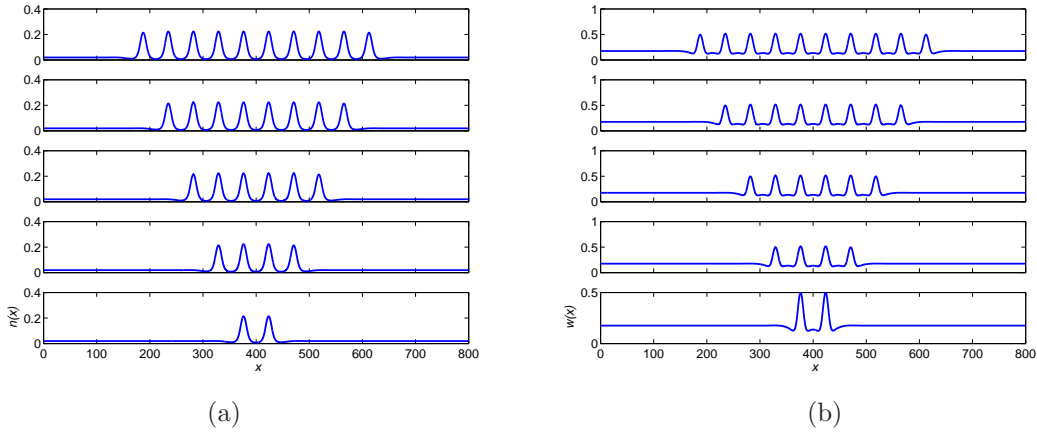
Figure 14: Localised equilibrium solutions (a) $n(x)$ and (b) $w(x)$ for the von Hardenberg model (6) - (7) at the points indicated by the black diamonds in figure 12(b). Solution shown, for parameter values are $\gamma = \sigma = 1.6$, $\mu = 0.2$, $r = 2.5$, $\delta = 30$. Computed in a domain of size $L = 400$, using Neumann boundary conditions.
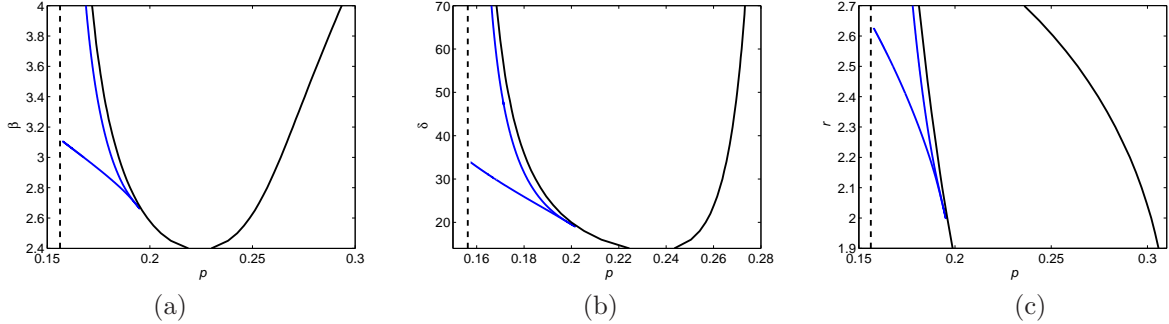
Figure 15: Regions of snaking behaviour and the location p_1 and p_2 of the pattern forming instabilities of $\mathcal{V}$ as two parameters are varied. (a) (p, β) plane, (b) (p, δ) plane, (c) (p, r) plane. Dashed vertical line indicates p_c, solid black lines indicate the pattern-forming instabilities of $\mathcal{V}$ denoted p_1 and p_2. Localised states exist inside the cusp-shaped region formed by the blue solid lines. For each case, the other parameters are held fixed at $\gamma = \sigma = 1.6$, $\mu = 0.2$, $\beta = 3$, $\delta = 30$, $r = 2.5$.

Figure 14 shows the form of the localised solutions for both $n(x)$ and $w(x)$, in (a) and (b) respectively. We note that the background state $\mathcal{V}$ has decreased, so that $n(x)$ becomes very small in the troughs between periods of the localised pattern. The form of $w(x)$ is particularly interesting since it clearly displays small humps between the large peaks, in a manner similar to the solutions of the reduced model shown in figure 9. Although the solutions at the two sides of the homoclinic snaking region are clearly slightly different in form, there appears to be little variation in wavenumber across the snaking region.

Figure 15 follows the location of the snaking region, as defined by following the location of saddle-node bifurcation points sufficiently far up the snake, as we vary p and a second parameter: β, δ or r; these are the parameters responsible for the strength of positive feedbacks in the model, and hence control the strength of the subcriticality. In each of figure 15(a-c) we show the locations of the pattern forming instabilities p_1 and p_2 as solid black curves that appear to meet just below the bottom edge of the plots. Within this convex region the $\mathcal{V}$ state is linearly unstable and we would expect stable space-filling periodic patterns to exist.

The solid blue curves bounding a cusp-shaped region on the left-hand side of each figure indicates the region within which localised patterns and homoclinic snaking exists. In each case, this snaking region terminates in a cusp that lies on the p_1 curve: at this point the pattern-forming instability along p_1 switches from being supercritical (at small values of β, δ and r) to being subcritical at larger values. As remarked on above, and illustrated in figure 12, spatially periodic patterns coexist with the localised patterns (although the localised pattern region may extend slightly further to the left than the periodic patterns); in figure 15 we do not show the location of the saddle-node bifurcation that marks the lower limit of existence of periodic patterns. Finally, the vertical dashed lines in figure 15 indicate the value of p_c at which the $\mathcal{V}$ state collides with the $\mathcal{B}$ state and ceases to exist. This vertical dashed line in addition appears to cause the localised states also to cease to exist.

Near to a codimension-two point at which the pattern forming instability changes from being supercritical to being subcritical, the homoclinic snaking structure emerges in a cusp-shaped region of parameter space.

5 Discussion

In this paper we have presented numerical and theoretical analysis of patterned solutions to the reaction-diffusion model (6) - (7) for vegetation growth in a semi-arid landscape proposed by von Hardenberg et al [9]. This model is an extension of the model proposed earlier by Klausmeier [12], and included above as equations (4) - (5). The model treats the interaction between only two variables: the vegetation level $n(x, t)$ and the soil water content $w(x, t)$. Importantly, it includes new terms that describe (i) the positive feedback effect in which vegetation preserves soil water through shading that restricts evaporation, (ii) the diffusion of water through the soil, and (iii) the manner in which vegetation restricts the diffusion of soil water through the root structure altering the effective diffusivity of the soil. We did not include the advection term that Klausmeier proposed to model the effect of sloping ground: all our results here are for horizontal ground and are in only one spatial dimension. Although the von Hardenberg model is

a useful extension of the Klausmeier model, we have noted that some of the terms are liable to change sign and hence to describe unphysical effects. These parameter regimes should be avoided. As a result we have found it most useful to consider states with small biomass amplitude and to analyse in detail the transitions between the bare ground state $\mathcal{B}$, the uniform vegetation state $\mathcal{V}$, and patterned states bifurcating from $\mathcal{V}$.

In our presentation we have focussed on the effect of varying these new feedback parameters, and the resulting bifurcation structures. In particular, the inclusion of these feedback parameters allows the uniform vegetation state $\mathcal{V}$ in the model to display a subcritical pattern forming instability, even when the bifurcation from $\mathcal{B}$ to $\mathcal{V}$ is supercritical. Moreover, we find that the localised states exist over a region of parameter space that appears to fill almost all the region between the initial bifurcation (at p_c) in which the $\mathcal{V}$ state appears, and the pattern-forming instability of $\mathcal{V}$ at p_1. This is different to the usual bifurcation structure found in the Swift–Hohenberg equation in the sense that, for that equation, homoclinic snaking is restricted to a smaller interval that lies between the linear instability (at p_1 here) and the saddle-node bifurcations on the branches of spatially periodic solutions. For the von Hardenberg model, the homoclinic snaking curves appear to extend very close to the saddle-node bifurcation for periodic patterns, and perhaps very slightly beyond it, see figure 12(b). At the other end, the snaking curves extend close to p_1, as can be seen in figure 15.

It is therefore tempting to suggest that the equilibrium localised patterns are, for this model, a clear indicator of the transition between the $\mathcal{B}$ state (in which there is no vegetation) and the state of spatially periodic pattern formation. At yet higher precipitation levels the spatially periodic patterns give way in turn to uniform, higher levels of vegetation. The fact that the homoclinic snaking curves extend over almost all the region in which subcritical patterns exist indicates that stationary patches of pattern will be 'pinned' throughout this region and we are less likely to see growing or shrinking fronts between periodic vegetated states and bare ground: the interface between them will be an equilibrium and so will not move, at least in the deterministic setting of the present paper. The effect of noise on the dynamics is not clear and would be of interest to consider in future work.

Given that the aim of this paper is to consider the influence of a number of new terms, involving additional parameters, it is very useful to have identified the new limit $\delta \gg 1$ in which we simplify the model through treating the diffusivity of soil water as occurring on an asymptotically much more rapid time scale, for small amplitude solutions near the critical precipitation value p_c at which the model is first able to sustain a uniform small-amplitude vegetation state. This greatly facilitates the analytic calculations, as well as being a limit that is biologically extremely relevant. It is perhaps surprising that it has not been noted previously, and we expect that it will help to organise a more thorough comparison of the generic features of a number of classes of model of this kind.

The reduced model in the limit $\delta \gg 1$ explains the behaviour near p_c for all biologically-relevant values of δ. Through weakly nonlinear analysis of this reduced model we see that the bifurcation in which $\mathcal{V}$ is created can be subcritical or supercritical. When it is supercritical, the expected case, we find that the subsequent pattern-forming instability is subcritical except in a very narrow range of parameter space. From this analysis of the reduced model, capturing the behaviour of small amplitude states, we conclude that for typical values of the feedback parameters β, δ and r the small amplitude behaviour is likely to involve homoclinic snaking (since it is strongly subcritical). This was that subsequently confirmed through numerical continuation of the full model and the results presented above in section 4.

The work presented here is therefore complementary to the recent work by Sherratt and co-authors, e.g. [21, 22, 23], and by van der Stelt and co-authors [25] on the original Klausmeier model: Sherratt has examined the existence and dynamics of travelling wave solutions whereas van der Stelt et al focus on the 'Busse balloon' of equilibrium states and investigate patterns of long wavelengths that becomes increasingly localised, but through a different mechanism, as the precipitation decreases. By focussing on the von Hardenberg model and the inclusion of additional feedback effects, the work presented here contributes to the general formulation and investigation of reaction-diffusion type models for this important biological scenario. It also confirms the existence of localised patterns, as proposed by Meron [18], when the positive feedbacks in the model are sufficiently strong.

Acknowledgements

References

[1] G. Bel, A. Hagberg and E. Meron, Gradual regime shifts in spatially extended ecosystems. *Theor. Ecol.* **5**,591-604 (2012)

[2] J. Burke and E. Knobloch, Localized states in the generalized Swift–Hohenberg equation. *Phys. Rev. E* **73**, 056211 (2006)

[3] J. Burke and J.H.P. Dawes, Localised states in an extended Swift–Hohenberg equation. *SIAM J. Appl. Dyn. Syst.* **11**, 261–284 (2012)

[4] A.S. Dagbovie and J.A. Sherratt, Pattern selection and hysteresis in th Rietkerk model for banded vegetation in semi-arid environments. *J. R. Soc. Interface* **11**: 20140465 (2014)

[5] J.H.P. Dawes, The emergence of a coherent structure for coherent structures: localized states in nonlinear systems. *Phil. Trans. R. Soc. Lond.* A **368**, 3519–3534 (2010)

[6] E.J. Doedel, A.R. Champneys, T. Fairgrieve, Y. Kuznetsov, B. Oldeman, R. Paffenroth, B. Sandstede, X. Wang and C. Zhang, AUTO-07p: continuation and bifurcation software for ordinary differential equations. Available online at `http://indy.cs.concordia.ca/auto/` (2011)

[7] E. Gilad, J. von Hardenberg, A. Provenzale, M. Shachak and E. Meron, A mathematical model of plants as ecosystem engineers. *J. Theor. Biol.* **244**, 680–691 (2007)

[8] K. Gowda, H. Riecke, and M. Silber, Transitions between patterned states in vegetation models for semiarid ecosystems. *Phys. Rev. E* **89**, 022701 (2014)

[9] J. von Hardenberg, E. Meron, M. Shachak, and Y. Zarmi, Diversity of vegetation patterns and desertification. *Phys. Rev. Lett.* **87**, 198101 (2001)

[10] R. Hille Ris Lambers, M. Rietkerk, F. van den Bosch, H. Prins and H. de Kroon, Vegetation pattern formation in semi-arid grazing systems. *Ecology* **82**, 50–61 (2001)

[11] B.J. Kealy and D.J. Wollkind, A nonlinear stability analysis of vegetative Turing pattern formation for an interaction-diffusion plant-surface water model system in an arid flat environment. *Bull. Math. Biol.* **74**, 803–833 (2012)

[12] C.A. Klausmeier, Regular and irregular patterns in semiarid vegetation. *Science* **284**(5421), 1826–1828 (1999)

[13] O. Lejeune, M. Tlidi and P. Couteron, Localized vegetation patches: a self-organised response to resource scarcity. *Phys. Rev. E* **66**, 010901(R) (2002)

[14] J.A. Mabbutt and P.C. Fanning, Vegetation banding in arid Western Australia. *J. Arid Environments* **12**, 41–59 (1987)

[15] W.A. MacFadyan, Soil and vegetation in British Somaliland. *Nature* **165**(4186), 121 (1950)

[16] W.A. MacFadyan, Vegetation patterns in the semi-desert planes of British Somaliland. *Geographical Journal.* **116**, 199–211 (1950)

[17] R.O. Meeuwig, Infiltration and soil erosion as influences by vegetation and soil in northern Utah. *J. Range Management* **23**, 185–188 (1970)

[18] E. Meron, Pattern-formation approach to modelling spatially extended ecosystems. *Ecol. Modelling* **234**, 70–82 (2012)

[19] C. Montana, J. Lopez–Portillo and A. Mauchamp, The response of two woody species to the conditions created by a shifting ecotone in an arid ecosystem. *J. Ecology* **78**, 789–98 (1990)

[20] M. Rietkerk, M.C. Boerlijst, F. van Langevelde, R. HilleRisLambers, J. van de Koppel, L. Kumar, H.H.T. Prins and A.M. de Roos, Self-organisation of vegetation in arid ecosystems. *Am. Nat.* **160**, 524–530 (2002)

[21] J.A. Sherratt, An analysis of vegetation stripe formation in semi-arid landscapes. *J. Math. Biol.* **51**, 183–197 (2005)

[22] J.A. Sherratt and G.J. Lord, Nonlinear dynamics and pattern bifurcations in a model for vegetation stripes in semi-arid environments. *Theor. Pop. Biol.* **71**, 1–11 (2007)

[23] J.A. Sherratt, Pattern solutions of the Klausmeier model for banded vegetation in semi-arid environments I. *Nonlinearity* **23**, 2657–2675 (2010)

[24] K. Siteur, E. Siero, M.B. Eppinga, J.D.M. Rademacher, A. Doelman and M. Rietkerk, Beyond Turing: the response of patterned ecosystems to environmental change. *Ecol. Complexity* **20**, 81–96 (2014)

[25] S. van der Stelt, A. Doelman, G. Hek, J.D.M. Rademacher, Rise and Fall of periodic patterns for a generalised Klausmeier–Gray–Scott model. *J. Nonlin. Sci.* **10**, 1432–1467 (2012)

[26] Y.R. Zelnick, S. Kinast, H. Yizhaq, G. Bel and E. Meron, Regime shifts in models of dryland vegetation. *Phil. Trans. R. Soc.* A **371**: 20120358 (2013)

[27] F.-L. Zheng, Effect of vegetation changes on soil erosion on the Loess Plateau. *Pedosphere.* **16**, 420–427 (2006)